Hindawi
Shock and Vibration
Volume 2018, Article ID 6905073, 11 pages
https://doi.org/10.1155/2018/6905073

Research Article

Numerical and Experimental Identification of Seven-Wire Strand Tensions Using Scale Energy Entropy Spectra of Ultrasonic Guided Waves

Ji Qian,[1] Xin Chen,[1] Limin Sun,[2] Guowen Yao,[1] and Xu Wang [1]

[1] *State Key Laboratory Breeding Base of Mountain Bridge and Tunnel Engineering, Chongqing Jiaotong University, Chongqing 400074, China*
[2] *College of Civil Engineering, Tongji University, Shanghai 200092, China*

Correspondence should be addressed to Xu Wang; xuwang@cqjtu.edu.cn

Received 16 January 2018; Accepted 26 February 2018; Published 5 April 2018

Academic Editor: Emanuele Reccia

Accurate identification of tension in multiwire strands is a key issue to ensure structural safety and durability of prestressed concrete structures, cable-stayed bridges, and hoist elevators. This paper proposes a method to identify strand tensions based on scale energy entropy spectra of ultrasonic guided waves (UGWs). A numerical method was first developed to simulate UGW propagation in a seven-wire strand, employing the wavelet transform to extract UGW time-frequency energy distributions for different loadings. Mode separation and frequency band loss of $L(0, 1)$ were then found for increasing tension, and UGW scale energy entropy spectra were extracted to establish a tension identification index. A good linear relationship was found between the proposed identification index and tensile force, and effects of propagation distance and propagation path were analyzed. Finally, UGWs propagation was examined experimentally for a long seven-wire strand to investigate attenuation and long distance propagation. Numerical and experimental results verified that the proposed method not only can effectively identify strand tensions but can also adapt to long distance tests for practical engineering.

1. Introduction

As the crucial component bearing tensile loads, steel strands can efficiently improve concrete crack resistance and are commonly employed for prestressed concrete structures, cable-stayed bridges, hoist elevators, and so forth. However, tensile force is difficult to maintain at design levels within strands over time, because of stretching, material characteristics, and various practical circumstances. Tension increases or decreases can lead to decreased bearing capacity and potentially cause major safety incidents [1].

Many studies have investigated steel strand tension, mainly based on optical fiber, magnetoelasticity, magnetic flux leakage (MFL), and ray path methods. Lan et al. [2, 3] developed fiber Bragg grating (FBG) intelligent steel strands to monitor lifecycle prestress and subsequently monitored prestress losses in reinforced concrete beams. They showed that intelligent steel strands can effectively provide prestressed time history and spatial distributions. However, the optical fiber(s) must be embedded in advance. Therefore, the method cannot be used for current in-service steel strands. Wang et al. [4, 5] used a magnetoelastic method to estimate steel strand tensions and considered calibration tests, engineering tests, and temperature compensation. However, test sections must be demagnetized many times prior to repeated measurements. It is difficult to ensure the material state after demagnetization is consistent with the initial state; hence the measurement results may be significantly affected by the demagnetization process. Krause et al. [6] and Mandache [7] used MFL signals to identify stress concentration regions and analyzed the influence of stress and geometry on MFL. However, this method can be applied to accessible components,

such as external prestressing strands or bridge cables and cannot be used to identify strand tensions for cables or strands imbedded in concrete. Ogilvie [8] proposed an X-ray based stress analysis method assuming the material was homogeneous and isotropic. Although this method is widely used to identify residual stress [9, 10], application for steel strand tension identification has been only rarely reported. The test is extremely expensive and has significantly human health impacts and other potential safety issues.

Ultrasonic guided wave (UGW) is a structural nondestructive detection method widely studied in recent years, because UGWs are formed by multiple reflections at the waveguide boundary. Therefore, UGW propagation characteristics are strongly affected by boundary conditions and local media defects, compared with body waves used for traditional ultrasonic testing, and can effectively provide waveguide defect characteristics and mechanical boundary variation. Thus, UGW based methods have been widely used for defects detection, for example, in bolts [11], pipes [12], and plates [13].

However, UGW propagation in strands is somewhat more complex than bolts, pipes, or plates. Kwun et al. [14] used UGW propagation to show experimentally that frequency band loss of first-order longitudinal guided waves ($L(0,1)$) in strands was caused by tension and defined the center frequency of the missing band as the notch frequency. Laguerre et al. [15] developed a low frequency ultrasonic reflectance magnetic elastic device to identify multiple UGW modes and dispersion in strands and also identified $L(0,1)$ frequency band loss. Treyssède and Laguerre [16] obtained UGW dispersion curves for seven-wire strands using a semianalytical finite element method based on simplified contact between wires and proposed a mode related to the notch frequency. Bartoli et al. [17] used finite elements to simulate UGW propagation in a seven-wire strand and employed two-dimensional Fourier transforms to identify UGW modes. They also identified $L(0,1)$ modal separation, caused by prestressing. Liu et al. [18] developed a dispersive expression for first-order screws using helical coordinates and analyzed spiral geometric parameter influences.

Strands are assembled in spiral and straight wires, and UGWs have a complex energy transfer between the wires due to mutual coupling; hence strand waveguide must be treated significantly different from spiral and straight wires. The main factor affecting the coupling state between wires is the contact stress caused by axial tensile force in the strands. Therefore, UGW propagation in strands includes tension effects, but it is extremely difficult to find a feature to characterize tension magnitude from complex UGW signals, although this would be greatly desired for engineering applications. Rizzo and Lanza di Scalea [19, 20] studied UGW propagation in a seven-wire strand at different stress levels using laser ultrasound and showed the UGW energy transmission spectrum has high sensitivity for tensile force. Peak frequency, amplitude, and area of the UGW energy transfer spectrum was used to identify tension. Bartoli et al. [21] used semianalytical finite elements to investigate tension and UGW energy transfer relationships between wires in a seven-wire strand. They proposed that the energy ratio between wires was significantly affected by increased tensile force, but no clear relationship between UGW energy ratio and tension was derived. Chaki and Bourse [22] studied the relationship between UGW velocity and tension using acoustic elasticity theory and proposed optimal excitation mode and frequency suitable for strand tension detection. However, UGW velocity is insensitive to strand tensile force, and the proposed approach can only be applied to tension recognition for strands with high strength strands due to residual stress effects. Nucera and Di Scalea [23] experimentally investigated nonlinear UGW propagation in a seven-wire strand and found that higher harmonic wave amplitudes decrease with axial tension. They proposed that nonlinear contact between adjacent wires was the main factor causing nonlinear UGW behavior in strands and employed nonlinear UGW was to monitor loading, including wrapping concrete effects. Liu et al. [24] used $L(0,1)$ characteristic frequency and frequency band notch peak ratio to test strand tension and corrected the relationship between the band notch center frequency and tension. However, propagation distance was not considered in the experimental results and the notch frequency is not explained by current theories.

Most previous studies have focused on identifying high tension strands and have poor recognition accuracy for low tension strands. Thus, although they are suitable for prestress loss evaluation where the strand still has large pulling force, the whole process of tension variation cannot be constantly monitored. Propagation effects have also been almost entirely ignored. Nevertheless, many studies have shown that UGWs propagated in strands carry significant tension information, but further studies are required to identify suitable tension identification method(s) for the wide range of practical conditions.

The current study selected seven-wire steel strands, commonly used in engineering structures, as the research object, and used UGW scale energy entropy spectra to identify steel strand tensions. Section 2 uses a continuous wavelet transform (CWT) to extract the UGW time-frequency energy distribution and defines the UGW scale energy entropy spectrum. Section 3 employs finite elements to simulate UGW propagation in a seven-wire strand, using the proposed CWT to obtain scale energy entropy spectra under different tension states. The UGW scale energy entropy spectra are then used eigenvectors to construct an identification index, and the effects of propagation distance and path are analyzed. Section 4 investigates UGW propagation experimentally in a seven-wire strand to verify proposed tension identification method. Section 5 summarizes and concludes the paper.

2. Ultrasonic Guided Wave Energy Entropy Spectrum

2.1. Time-Frequency Energy Analysis. Let the UGW signal be $f(t) \in L(R)$; then the CWT is defined as

$$W_f(m,n) = \int_R f(t) \cdot \overline{\psi_{m,n}(t)}\, \mathrm{d}t, \tag{1}$$

where $\overline{\psi_{m,n}(t)}$ is the complex conjugate of basis wavelet $\psi_{m,n}(t)$, which is obtained by translation and expansion of the mother wavelet, $\psi(t)$:

$$\psi_{m,n}(t) = \frac{1}{\sqrt{|m|}} \cdot \psi\left(\frac{t-n}{m}\right), \tag{2}$$

where m and n are scale and time factors, respectively; and $\psi(t)$ must meet

$$C_\psi = \int_{-\infty}^{\infty} \frac{|\Psi(w)|^2}{|w|} \mathrm{d}w < \infty, \tag{3}$$

where $\Psi(w)$ is the Fourier transform of $\psi(t)$.

Applying Fourier transform, (1) can be expressed in the frequency domain as

$$W_f(m,n) = \frac{1}{\sqrt{m}} \int_R F(w) \cdot \overline{\Psi(mw)} \cdot \mathrm{e}^{jwn}\, \mathrm{d}w, \tag{4}$$

where $F(w)$ is the Fourier transform of $f(t)$ and $\overline{\Psi(mw)}$ is the complex conjugate of $\Psi(mw)$.

Since $\psi(t)$ and $\psi(w)$ are window functions of the time and frequency domains, respectively, smaller window width provides higher resolution in the CWT time-frequency window. From the Heisenberg uncertainty principle, time and frequency domain windows are mutually restricted, and the same basis wavelet cannot be simultaneously limited in both time and frequency domains. Therefore, the wavelet time-frequency window has higher frequency resolution in low frequency bands and has higher temporal resolution in high frequency bands. Thus, multiple resolution analysis means CWT can effectively extract small signal changes and has been widely used for fault detection and diagnosis of dynamic systems [25, 26].

The Morlet wavelet is a complex exponential function under a Gaussian envelope, which has advantages of small time-frequency window area, strong localization in the time-frequency domain, and good symmetry. Therefore, the complex Morlet wavelet was adopted as the mother wavelet for CWT. $\psi(t)$ center time, $\psi(t)$ center frequency, $\psi(t)$ time window width, and $\psi(t)$ frequency band width were assumed to be t_c, f_c, t_b, and f_b, respectively. When $t = n$, the UGW time-frequency energy distribution can be obtained in a time-frequency window with time and frequency lengths TL and FL:

$$\mathrm{TL} = \left[mt_c + n - \frac{mt_b}{2}, mt_c + n + \frac{mt_b}{2}\right], \tag{5}$$

$$\mathrm{FL} = \left[\frac{f_c}{m} - \frac{f_b}{2m}, \frac{f_c}{m} + \frac{f_b}{2m}\right], \tag{6}$$

respectively. The energy density of the entire UGW signal, $M(m,n)$, for any time-scale can be obtained by translation and expansion of m and n, that is,

$$M(m,n) = \left|W_f(m,n)\right|^2, \tag{7}$$

and the UGW time-frequency energy matrix can be expressed as

$$\mathrm{TFR} = \begin{bmatrix} M(1,1) & \cdots & M(1,n) \\ & \cdots & \\ M(m,1) & \cdots & M(m,n) \end{bmatrix}. \tag{8}$$

2.2. Scale Energy Entropy Spectrum. The amplitude spectrum of a signal is assumed to be a discrete random variable $\{X\} = \{x_1, x_2, \ldots, x_N\}$, and the Shannon entropy [27] of X is defined as

$$H(X) = -\sum_{i=1}^{N} P_i \cdot \log_e(P_i), \tag{9}$$

where $P_i = x_i / \sum_{i=1}^{N} x_i$, $\sum_{i=1}^{N} P_i = 1$, and $i = 1, 2, \ldots, N$.

The UGW time-frequency energy matrix shown in (8) can be expressed as a column vector:

$$\mathrm{TFR}(m) = \begin{Bmatrix} M(1,\eta) \\ \vdots \\ M(m,\eta) \end{Bmatrix}, \quad (\eta = 1, 2, \ldots, n), \tag{10}$$

where $M(1,\eta)$ and $M(m,\eta)$ are the change between the energy of UGWs and time when the scale is 1 and m, respectively.

Any element in TFR can be regarded as a set of random variables, and the Shannon entropy of every element can be calculated from (9). Thus, the scale energy entropy spectrum is

$$\mathbf{H}(m) = \begin{Bmatrix} H(M(1,\eta)) \\ \cdots \\ H(M(m,\eta)) \end{Bmatrix}, \tag{11}$$

where $H(M(1,\eta))$ and $H(M(m,\eta))$ are the Shannon entropy of $M(1,\eta)$ and $M(m,\eta)$, respectively.

The UGW complexity at different decomposition levels in the time domain can be effectively described by **H**. Compared with traditional time-frequency [28] and wavelet [29] entropy, **H** characterizes UGW signals more precisely and is more sensitive to dynamic UGW changes due to full utilization of information from combined time and frequency analysis.

Since there is mutual contact between adjacent wires, a complex energy transfer relationship is generated by UGW propagation. At different loading levels, contact state discrepancies alter UGW transfer characteristics, providing further sensitivity to the time-frequency domain energy distribution, and entropy is altered accordingly. Therefore, we adopted **H** as the eigenvector to construct the tension identification index.

3. Numerical Simulation

3.1. Numerical Setup. Propagation of UGWs in a seven-wire strand was numerically simulated by the ABAQUS/explicit

Table 1: Strand geometric and material parameters adopted for numerical analysis.

Geometric parameter		Material parameter	
Center wire diameter, d_c (mm)	5.08	Young's modulus, E (GPa)	196
Peripheral wire diameter, d_h (mm)	5.08	Poisson's ratio, v	0.29
Strand diameter, d (mm)	15.2	Density, ρ (kg/m^3)	7850
Peripheral pitch, h (mm)	230	Yield load, F (kN)	203
Peripheral twist angle, β (°)	7.9	Ultimate tensile stress, UTS (MPa)	1860

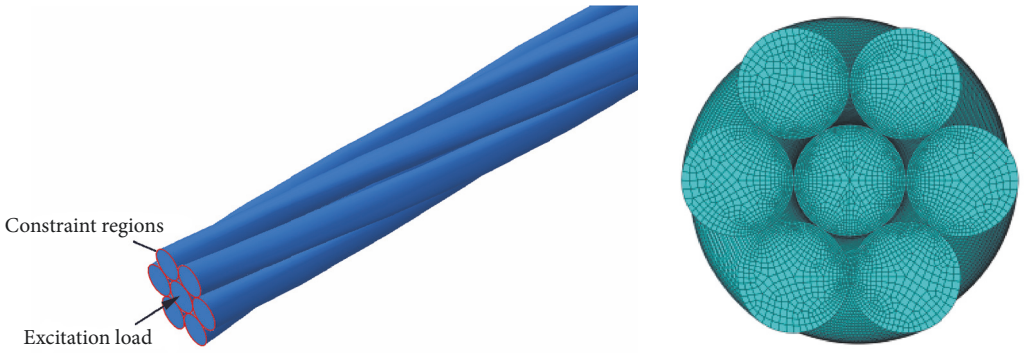

(a) Excitation load and the boundary condition (b) Finite element mesh

Figure 1: Finite element model for the seven-wire strand.

time-transient solver with strand length $L = 0.52$ m and material damping was not considered. Table 1 shows the strand geometric and material parameters.

Finite element model (FEM) mesh size is usually imposed by the minimum UGW wavelength. Accurate calculation of the volatility effect requires every wavelength to have at least 8 calculation nodes [30], and the recommended element size is

$$\text{RES} = \Delta l \leq \frac{\lambda_{\min}}{n-1}, \tag{12}$$

where $n = 8$. The highest frequency ($f_{\max}$) considered was 500 kHz, and transverse wave velocity (C_T) = 3130 m/s in steel; hence

$$\text{RES} = \Delta l \leq \frac{\lambda_{\min}}{8-1} = \frac{c_T}{7 \times f_{\max}} = 0.92\,\text{mm}. \tag{13}$$

Mesh size was reduced near contact regions to better simulate contact between adjacent wires. Therefore, the element size in the axial direction was chosen as RES = 1 mm (slightly above 0.92 mm), and the minimum element size in the contact regions was RES = 0.1 mm. The final FEM mesh comprised 1,745,623 linear hexahedral 8 node elements. Figure 1 shows the finite element model for the seven-wire strand.

The time integral step is another significant factor in controlling precision. A structure's dynamic response can be considered a combination of each vibration mode, and the minimum time integral step should be sufficient to solve the highest order vibration mode. Thus, the time integral step is typically required to be less than 1/20 of the minimum period in the finite element solution for transient dynamics problems. Automatic time integral step was applied due to the strand complexity.

Normal and tangential contacts between wires were simulated using hard contact and friction, respectively. The friction coefficient was defined as 0.6. To simulate anchorages, all displacements were constrained at one end, and all displacements aside from axial direction displacements were constrained at the other end to apply tension and excitation. The constraint regions were the edge of the wire end face.

The simulation process consisted of three stages.

Stage 1 (applying axial tension). Tension is applied to the end where axial displacement is permitted. To prevent interference signal generation, the applied tension amplitude curve should be as smooth as possible and over suitable time frame. We selected the time frame as 300 μs, and Figure 2 shows the loading amplitude curve.

Stage 2 (excitation). We employed a triangular pulse as the excitation load with excitation time = 3 μs, as shown in Figure 3. The excitation load was axially applied to the center node of the center wire.

Stage 3. Simulating UGW propagation in the strand required 697 μs after completing Stage 2.

3.2. Time-Frequency Energy Analysis. The UGW time-frequency energy matrices were obtained by wavelet transform to axial acceleration signals at the center node of end face in the center wire, with decomposition scale = 128. Figure 4 shows contour maps of the time-frequency energy distribution at different tensions compared with theoretical time-frequency curves of free wire.

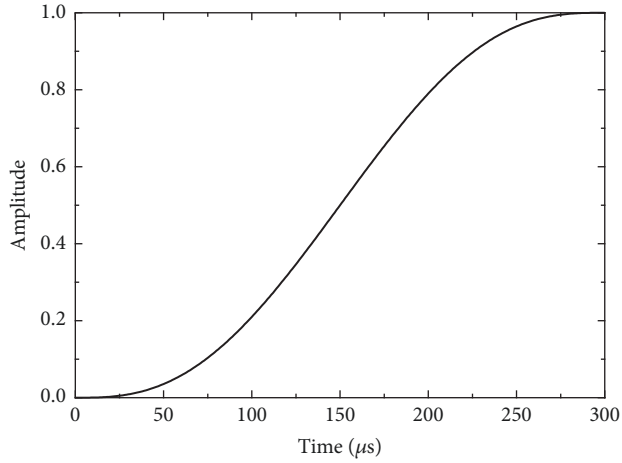

Figure 2: Loading time-history curve.

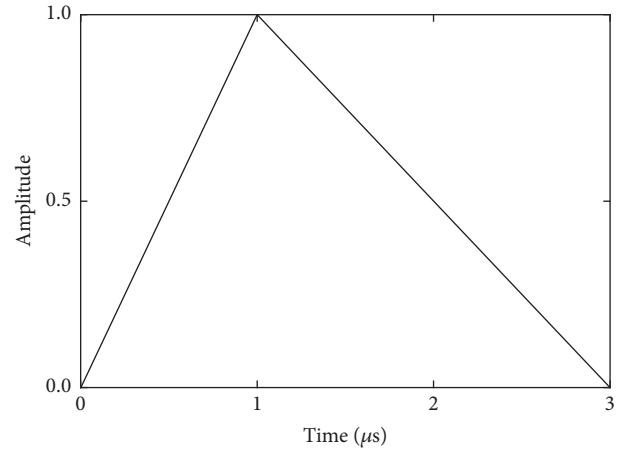

Figure 3: Excitation load.

Peripheral steel wire without tension (Figure 4(a)) has a weaker restraining effect on the center steel wire, and the center wire boundary conditions are basically similar to free wires. Thus, UGW modal distribution coincides well with the theoretical time-frequency curve of free wires, with the axial acceleration signal of the center node in the end of the central wire containing only $L(0,1)$. Low frequency $L(0,1)$ components arrive at the monitoring point after approximately 100 μs, and UGW energy is largely concentrated on 200–550 kHz. Two distinct echoes are evident, but their arrival time is earlier than the theoretical time-frequency curve, which suggests that UGWs with multiple reflections at the end surface in strands increases the propagation velocity. UGWs only need to meet circumferential surface boundary conditions before propagating to the end, following the theoretical time-frequency curve. However, the end surface boundary condition must be also met at every reflection, which increases propagation velocity.

When the strand tension was equivalent to 70% of the ultimate tensile stress (UTS), the restraining effect of the outer wire on the center wire was significantly strengthened, causing $L(0,1)$ modal separation (Figure 4(b)), significantly different from free wires. UGW energy was mainly concentrated in first waves, in approximately 300–500 kHz band, with a significant band loss at 550 kHz. Echo energy was also significantly reduced, and only one echo was evident.

3.3. Tension Identification Index. Section 3.2 verified that the time-frequency energy distribution was sensitive to UGW changes, because it not only reflects UGW energy distribution in the time-frequency domain, but also contains modal information. Figure 5 shows **H** calculated from (9) using the UGW time-frequency energy distribution for different tensions and normalized by dividing by the maximum value. Echoes are usually difficult to receive in practical engineering applications due to severe attenuation. Therefore, not all **H** considered end-echo impacts.

Figure 5 shows the effect on **H** from increasing strand tension. Significant **H** deviation is evident for scales 3–42 and 64–92, but other regions (scales 42–64 and 92–109) remain almost unchanged. This indicates that UGW energy transmission characteristics in the local frequency band can be affected by tensile force variations, and different frequency components have different sensitivity for stress boundary changes caused by tension. Thus, tension variations can be effectively reflected by **H**, but the precise relationship is difficult to quantify, and the tension in strands cannot be accurately determined.

The signal differences can be generally described by the eigenvector differences for these signals, using the eigenvector established at a tensile force as the reference. The deviation level between a tension which is waiting to be detected and a tension corresponding to the reference is vividly characterized by the differences of eigenvectors. Therefore, we defined the distance $D(P)$ between two vectors as a tension identification index:

$$D(P) = \left\| I_P - I_c \right\|, \tag{14}$$

where I_c and I_P are the reference and tension, P, eigenvectors, respectively.

Figure 6 shows $D(P)$ between **H** for different tensions, using **H** for 70% UTS as the reference, where K is the absolute value of the slope, and R^2 is the correlation coefficient of the fitted curve, respectively. The tension identification index, $D(P)$, changes monotonically and approximately linearly with tensile force. Thus, eigenvector difference provides an effective index to identify strand tension. Even if tension changes only slightly, $D(P)$ has a more significant variation for larger K. Therefore, K represents the sensitivity of the identification index to tension variation.

3.4. Propagation Distance. Propagation distance has a significant influence on UGW characteristics. Therefore, we investigated **H** for different locations, selecting the section center node at Z = 0.12, 0.135, and 0.52 m from the excitation point (Figures 6, 7(a), and 7(b), resp.) to eliminate influences from end surface echoes.

Figures 6 and 7 show similar linearity, with sensitivity (K) increasing by 21.46% from Z = 0.12–0.135 m, but only 5.63% from Z = 0.135–0.52 m; that is, sensitivity increases

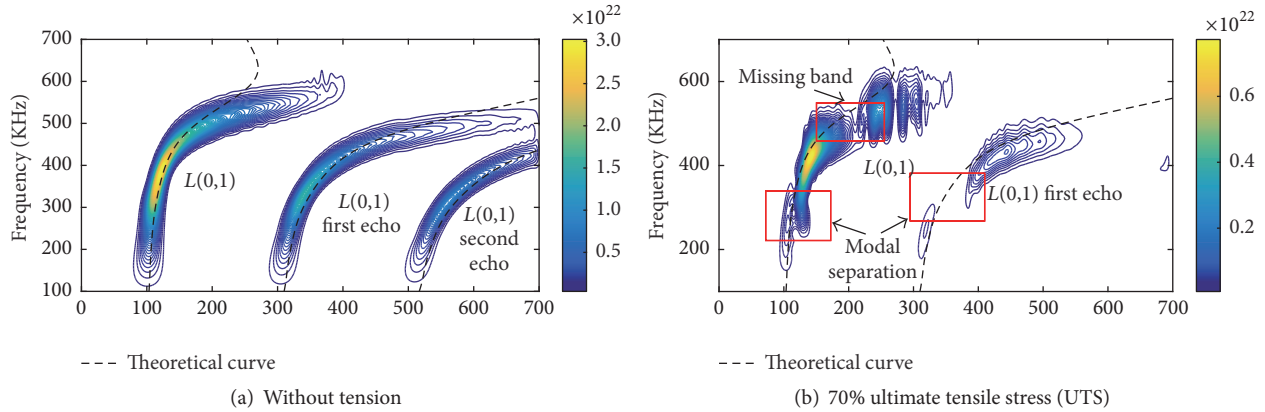

Figure 4: UGW time-frequency energy distribution.

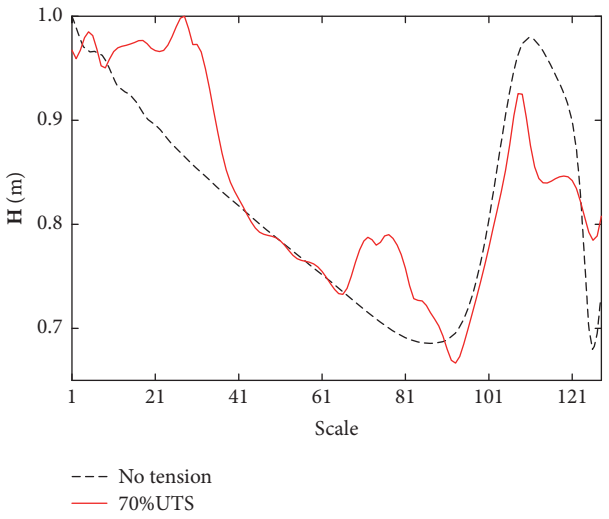

Figure 5: Scale energy entropy spectrum (**H**) for no tension and 70% UTS cases.

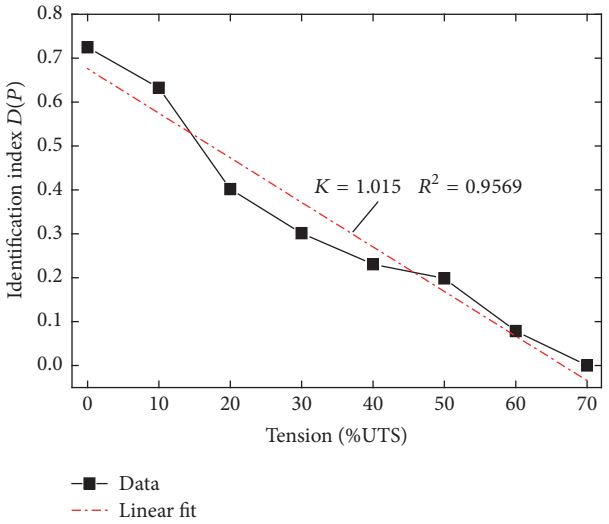

Figure 6: Proposed identification index and tension.

with increasing propagation distance, but the change is somewhat nonlinear with smaller increase for larger distance. The correlation coefficient (R^2) always exceeds 0.95. Contact information carried by UGWs is more abundant with longer propagation distance, which is the main reason for increased sensitivity.

3.5. Propagation Path. Propagation of UGWs in strands has multiple propagation paths due to mutual coupling of wires in strands. In the previous sections, UGW excitation and receiving points were located on the same wire, that is, the uncoupled propagation path. Propagation path effects can be estimated by ensuring that the excitation and receiving points are located on different wires.

Figure 8 shows the proposed identification index for the coupled propagation case, for the same propagation distance as Figure 6. The relationship between $D(P)$ and tension remains similar to Figure 6, and numerical results show reasonably good agreement to the fitted line (R^2 = 0.9696). However, K = 0.8188 and 19.33% is lower than the uncoupling propagation path, which is due to differences of contact information carried by the UGWs. In the uncoupled propagation path, guided waves are excited at the center wire, which propagates peripheral wires through contact regions between wires. Hence, it mutually transmits between center and peripheral wires with increasing transmission distance. Thus, UGWs carry contact information between all peripheral wires and the center wire. However, only contact information between wires to the excitation and receiving points were carried for the coupled propagation path. In contrast, UGWs following the uncoupled propagation path carry significantly more abundant contact information.

Although K for the coupled propagation path is lower than for the uncoupled path, linearity between the identification index and tension remains significant. Hence, the propagation path has little effect on linearity, and results from the coupled propagation path can be used to verify uncoupled path outcomes, to further ensure the accuracy and reliability of recognition results.

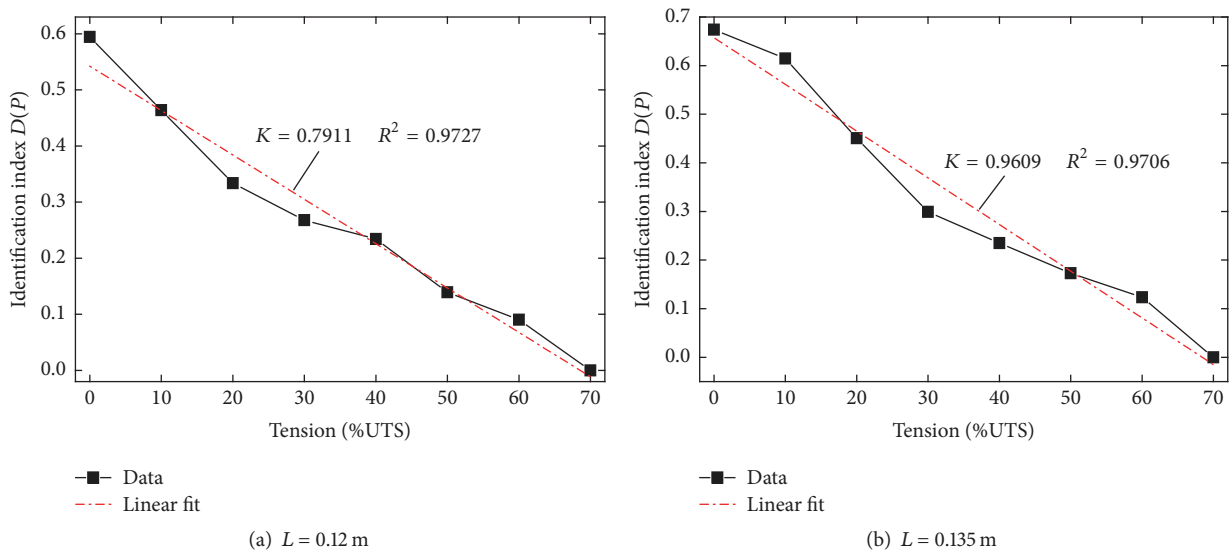

Figure 7: Effects of propagation distance on the proposed identification index ($D(P)$).

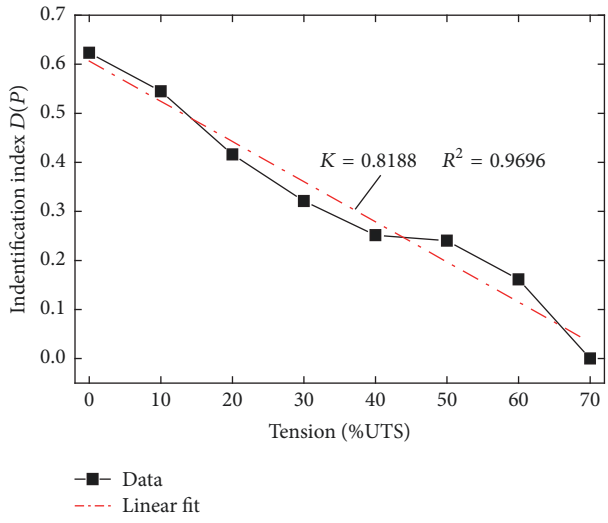

Figure 8: Proposed identification index for coupled propagation path.

4. Experimental Analyses

Attenuation is the basic UGW characteristic. UGWs have a wider wave packet when propagating longer distances, which can cause lower amplitude, and material damping can also reduce UGW energy. Calculation limitations meant only undamped short distance UGW propagation was considered for the FEM. However, test distances are usually significantly larger for actual engineering tests; hence UGW signals will have lower energy and narrower frequency band. Therefore, a long seven-wire strand was used for ultrasonic guided wave propagation experiments to investigate longer distance propagation influence on tension identification.

4.1. Experimental Setup for Loading in a Seven-Wire Strand. Large reaction walls and through-core hydraulic jacks were employed for the seven-wire strand loading experiment, as shown in Figure 9. The overall strand diameter = 15.2 mm and length = 5.5 m and other strand material parameters were consistent with the FEM analysis. One end of the strand was anchored, and the other was tensioned to maximum = 178.9 kN (70% UTS). Loading and unloading steps were 25.6 kN (10% UTS). A pressure sensor was placed between the hydraulic jack and the reaction wall to provide accurate loading data.

4.2. Experimental Setup for Ultrasound Guided Wave Propagation in a Seven-Wire Strand. The PCI-2 acoustic emission system produced by American PAC was selected to conduct the UGW long propagation experiment. The system frequency range was 0–4000 kHz, sensors were WD broadband piezoelectric transducers with testing frequency range 100–1000 kHz, and sampling rate was 2000 kHz. It is difficult to generate sufficient energy using the normal FEM triangular pulses due to material damping over the long strands. Therefore, to ensure high signal-to-noise ratio for the measured signals, a series of 100–700 kHz single cycle sinusoidal pulses with 2 kHz step frequency were selected as the excitation source:

$$f(t) = \sum_{i=0}^{f-f_0/\Delta f} V_i(t) \cdot \sin\left(2\pi\left(f_0 + \Delta f\right)\right), \quad (15)$$

where $V_i(t)$ is the rectangular window function; $f_0 = 100$ kHz, $f = 700$ kHz, $\Delta f = 2$ kHz are the minimum, maximum, and step frequencies, respectively; and the rectangle window length $T_i = 1/f_0 + i \cdot \Delta f$.

The excitation sensor was arranged on one end of the center wire and receiving sensors were arranged on the center

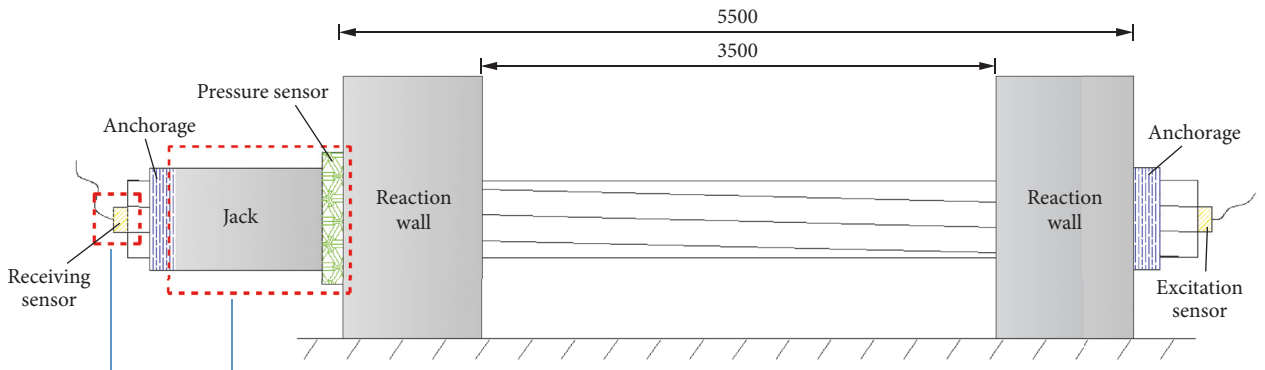

(a) Layout of experiment equipment (Unit: mm)

(b) Receiving sensors

(c) Hydraulic jack and pressure sensor

Figure 9: Long propagation experiment layout and pictures.

and helical wires, respectively. Each load is held for 2 min after loading; then the same excitation pulse was generated to excite UGWs in the strands. The measured waveforms were used for judging strand tensions.

4.3. Experimental Results. Figure 10 shows measured guided wave signals and corresponding time-frequency energy distributions of the receiving sensor at the center wire for minimum and maximum applied loads. UGW energy leakage from the central to outer wires becomes more significant with increasing tension due to increased contact forces between the wires. Thus, the UGW amplitudes decrease significantly with increasing tension.

Although a wide band is excited (100–1000 kHz), measured UGW energy is concentrated near 270 kHz, because UGW high frequency components are severely attenuated over the long propagation. For the zero tension case, UGW arrival time for the maximum energy is reasonably consistent with the theoretical time-frequency curve, and only $L(0,1)$ is included. In contrast, at 70% UTS, arrival time for the maximum energy is significantly offset from the theoretical time-frequency curve. The excitation source is a long duration signal, which causes overlap between measured UGWs, and there is no evident modal separation, as shown in Figure 10(b). Although the UGWs propagate the long distance, time-frequency energy distribution still shows significant differences for different loadings.

Figure 11 shows the relationships for $D(P)$ and tension under different propagation paths. $D(P)$ is broadly linear with tension, consistent with FEM results, and loading and unloading have little effects on this linearity.

Sensitivity for the uncoupled propagation path is 1.221, 60.19%, and 20.30% larger than that for the coupled propagation path and FEM results with short propagation path, respectively. This supports the FEM based conclusions that identification index has higher sensitivity for the uncoupled propagation path, and sensitivity is enhanced with increasing propagation distance.

Contacts between wires in the long propagation path experiment are somewhat different from the ideal state assumed for FEM analysis. The experimental UGWs only carry contact information between the central and outer wire for coupled propagation paths. Therefore, the local coupling state of the contact area has a large influence on the measured UGW, and hence coupled pathway sensitivity = 0.762 and 6.91% is lower than FEM results.

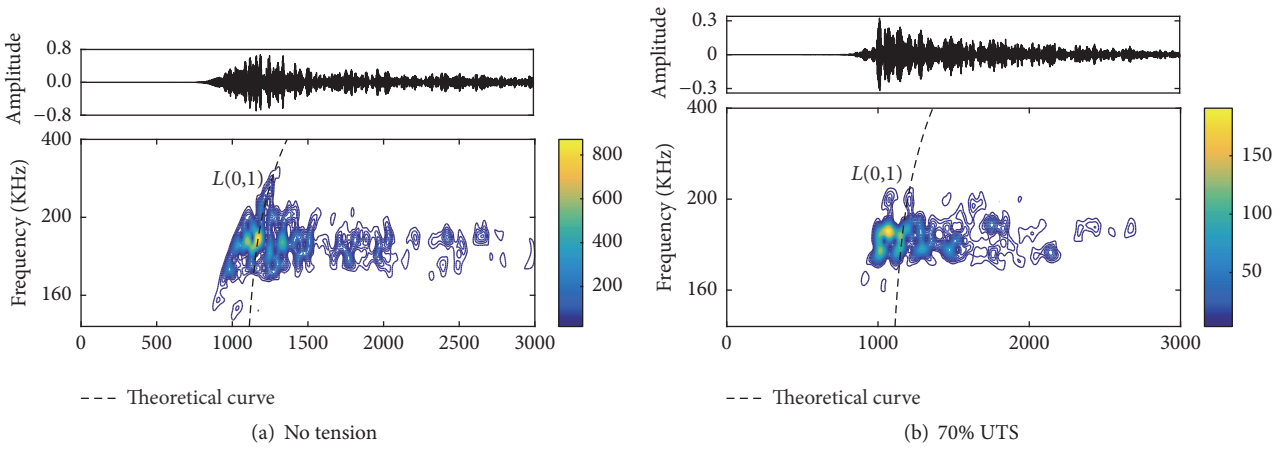

Figure 10: UGW time-frequency energy distribution.

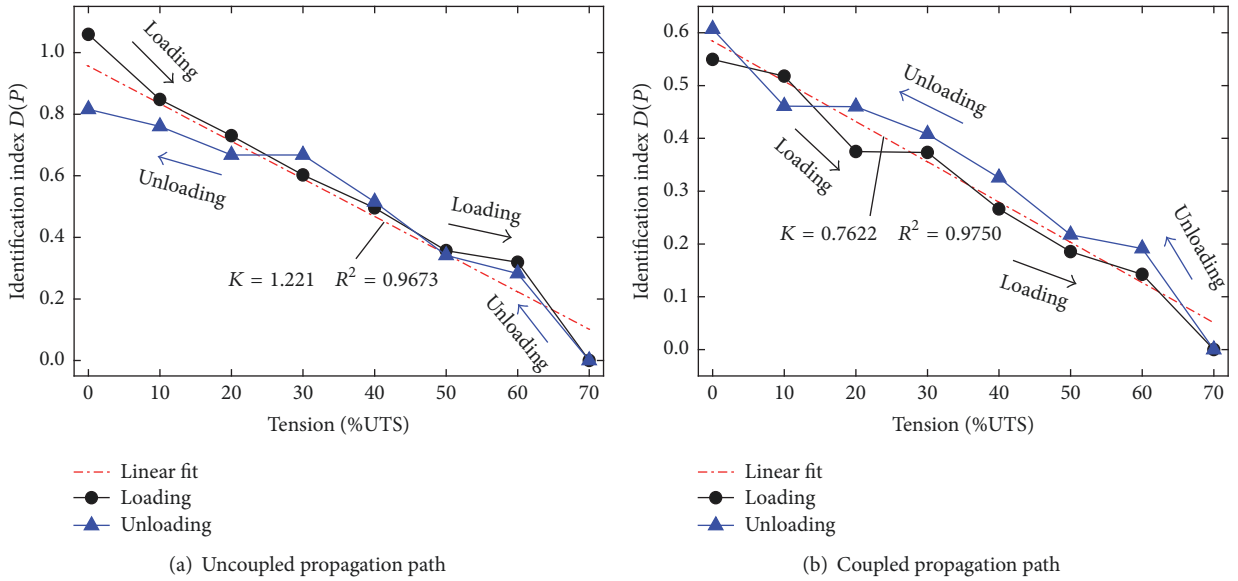

Figure 11: Proposed identification index and tension relationships for different long propagation pathways.

For both FEM and experimental results, K for coupled propagation paths decreases by 19.33% and 37.58% compared with uncoupled propagation paths, respectively. Compared with the decreased FEM amplitude, the decreased experimental amplitude increases by 94.41%. This discrepancy is because UGW propagation distance in the experiments was farther than that for FEM. Thus, as propagation distance increases, the propagation path has more significant impact on recognition results.

These outcomes confirm that that the proposed method could be used to identify tension in longer strands and would be suitable for practical engineering tests.

5. Conclusions

This study proposed a tension identification method for seven-wire strands. Numerical simulation and experimental measurements were employed to study tension effects on UGW propagation. A tension identification index based on UGW scale energy entropy spectra (**H**) was derived, and propagation distance and path effects were considered.

UGW time-frequency energy distribution shows significant differences for different loading levels, exhibiting $L(0, 1)$ modal separation and frequency band loss with increasing tensile force, mainly due to changing boundary conditions.

The variety of tension in strands has significant influence on **H**. The proposed identification index measures the distance between **H** vectors for the different tensions, which is strongly linearly dependent on tension ($R^2 > 0.95$). Experimental results were in good agreement with the numerical simulations.

The proposed identification index becomes more sensitive to tension as UGW propagation distance increases. However, this enhancement decreases with further propagation distance increase.

The proposed identification index can accurately identify strand tension for coupled and uncoupled paths, although the propagation path influences sensitivity to tension due to the different contact information carrying UGWs in the two cases. The effect of propagation path on sensitivity becomes more significant as propagation distance increases. Coupled path sensitivity (K) decreases by 19.33% and 37.58% (numerical simulation and experiment, resp.) compared to the uncoupled path. Thus, it is more effective in using the uncoupling propagation path to identify tension, and the coupling propagation path can be used to verify the uncoupling propagation path and ensure accuracy and reliability.

Conflicts of Interest

The authors declare that there are no conflicts of interest regarding the publication of this paper.

Acknowledgments

This research was supported by the National Natural Science Foundation of China (Grants 51478347 and 51408090) and the Chongqing Research Program of Basic Research and Frontier Technology (Grant cstc2015jcyjB0014).

References

[1] Z. P. Bažant, Q. Yu, and G.-H. Li, "Excessive long-time deflections of prestressed box girders. I: record-span Bridge in Palau and other paradigms," *Journal of Structural Engineering*, vol. 138, no. 6, pp. 676–686, 2012.

[2] C. Lan, Z. Zhou, and J. Ou, "Full-scale prestress loss monitoring of damaged RC structures using distributed optical fiber sensing technology," *Sensors*, vol. 12, no. 5, pp. 5380–5394, 2012.

[3] C. Lan, Z. Zhou, and J. Ou, "Monitoring of structural prestress loss in RC beams by inner distributed Brillouin and fiber Bragg grating sensors on a single optical fiber," *Structural Control and Health Monitoring*, vol. 21, no. 3, pp. 317–330, 2014.

[4] G. Wang, M. L. Wang, Y. Zhao, Y. Chen, and B. Sun, "Application of em stress sensors in large steel cables," in *Proceeding of SPIE, Smart Structures and Materials, International Society for Optics and Photonics*, vol. 5765, pp. 395–406, USA, March 2005.

[5] Y. Zhao and M. L. Wang, "Non-destructive condition evaluation of stress in steel cable using magnetoelastic technology," in *Proceedings of the of SPIE 6178, Nondestructive Evaulation for Health Monitoring & Diagnostics*, International Society for Optics and Photonics, 2006.

[6] T. W. Krause, R. W. Little, R. Barnes, R. M. Donaldson, B. Ma, and D. L. Atherton, "Effect of stress concentration on magnetic flux leakage signals from blind-hole defects in stressed pipeline steel," *Research in Nondestructive Evaluation*, vol. 8, no. 2, pp. 83–100, 1996.

[7] C. Mandache, "Magnetic flux leakage investigation of interacting defects: Stress and geometry effects," *Developments in Earth Surface Processes*, vol. 10, no. 6, pp. 235–247, 2007.

[8] R. E. Ogilvie, "A different approach to X-ray stress analysis," *Spectrochimica Acta Part B: Atomic Spectroscopy*, vol. 62, no. 6-7, pp. 529–532, 2007.

[9] E. Dobročka, P. Novák, D. Búc, L. Harmatha, and J. Murín, "X-ray diffraction analysis of residual stresses in textured ZnO thin films," *Applied Surface Science*, vol. 395, pp. 16–23, 2017.

[10] S. Lei, J.-H. Huang, and H. Chen, "Measurement of residual stress on TiN/Ti bilayer thin films using average X-ray strain combined with laser curvature and nanoindentation methods," *Materials Chemistry and Physics*, vol. 199, pp. 185–192, 2017.

[11] V. Madenga, D. H. Zou, and C. Zhang, "Effects of curing time and frequency on ultrasonic wave velocity in grouted rock bolts," *Journal of Applied Geophysics*, vol. 59, no. 1, pp. 79–87, 2006.

[12] H. Kwun, S. Y. Kim, H. Matsumoto, and S. Vinogradov, "Detection of axial cracks in tube and pipe using torsional guided waves," in *Proceedings of the 34th Annual Review of Progress in Quantitative Nondestructive Evaluation*, vol. 975, pp. 193–199, American Institute of Physics, USA, 2008.

[13] J. Wu, Z. Ma, and Y. Zhang, "A Time-Frequency Research for Ultrasonic Guided Wave Generated from the Debonding Based on a Novel Time-Frequency Analysis Technique," *Shock and Vibration*, vol. 2017, Article ID 5686984, 11 pages, 2017.

[14] H. Kwun, K. A. Bartels, and J. J. Hanley, "Effects of tensile loading on the properties of elastic-wave propagation in a strand," *The Journal of the Acoustical Society of America*, vol. 103, no. 6, pp. 3370–3375, 1998.

[15] L. Laguerre, M. Brissaud, and J.-C. Aime, "Low frequency ultrasound reflectometry device based on magneto-elastic transducers for the non-destructive evaluation of steel rods and cables," *Bulletin des Laboratories des Ponts et Chaussees*, no. 239, pp. 7–27, 2003.

[16] F. Treyssède and L. Laguerre, "Investigation of elastic modes propagating in multi-wire helical waveguides," *Journal of Sound and Vibration*, vol. 329, no. 10, pp. 1702–1716, 2010.

[17] I. Bartoli, G. Castellazzi, A. Marzani, and S. Salamone, "Prediction of stress waves propagation in progressively loaded seven wire strands," in *Proceedings of the Sensors and Smart Structures Technologies for Civil, Mechanical, and Aerospace Systems (SPIE '12)*, vol. 8345, USA, March 2012.

[18] Y. Liu, Q. Han, C. Li, and H. Huang, "Numerical investigation of dispersion relations for helical waveguides using the Scaled Boundary Finite Element method," *Journal of Sound and Vibration*, vol. 333, no. 7, pp. 1991–2002, 2014.

[19] P. Rizzo and F. Lanza di Scalea, "Wave propagation in multi-wire strands by wavelet-based laser ultrasound," *Experimental Mechanics*, vol. 44, no. 4, pp. 407–415, 2004.

[20] P. Rizzo, "Ultrasonic wave propagation in progressively loaded multi-wire strands," *Experimental Mechanics*, vol. 46, no. 3, pp. 297–306, 2006.

[21] I. Bartoli, R. Phillips, F. L. D. Scalea et al., "Load monitoring in multiwire strands by interwire ultrasonic measurements," in *Proceedings of the Smart Structures & Materials & Nondestructive Evaluation & Health Monitoring (SPIE)*, vol. 6932, p. 693209-1-693209-11, 2008.

[22] S. Chaki and G. Bourse, "Guided ultrasonic waves for non-destructive monitoring of the stress levels in prestressed steel strands," *Ultrasonics*, vol. 49, no. 2, pp. 162–171, 2009.

[23] C. Nucera and F. L. Di Scalea, "Monitoring load levels in multi-wire strands by nonlinear ultrasonic waves," *Structural Health and Monitoring*, vol. 10, no. 6, pp. 617–629, 2011.

[24] X. Liu, B. Wu, F. Qin, C. He, and Q. Han, "Observation of ultrasonic guided wave propagation behaviours in pre-stressed multi-wire structures," *Ultrasonics*, vol. 73, pp. 196–205, 2017.

[25] J. Seshadrinath, B. Singh, and B. K. Panigrahi, "Incipient turn fault detection and condition monitoring of induction machine using analytical wavelet transform," *IEEE Transactions on Industry Applications*, vol. 50, no. 3, pp. 2235–2242, 2014.

[26] F. Al-Badour, M. Sunar, and L. Cheded, "Vibration analysis of rotating machinery using time-frequency analysis and wavelet techniques," *Mechanical Systems and Signal Processing*, vol. 25, no. 6, pp. 2083–2101, 2011.

[27] C. E. Shannon, "A mathematical theory of communication," *Bell Labs Technical Journal*, vol. 27, pp. 379–423, 623–656, 1948.

[28] L. Xiaohua, H. Jing, L. Vue, and W. Zhiqi, "Fault current identification of DC traction power supply system based on lmd time-frequency entropy," in *Proceedings of the IEEE International Conference on Power and Renewable Energy, ICPRE '17*, pp. 237–240, Shanghai, China, October 2017.

[29] L. G. Li, G. X. Liu, and C. Y. Hu, "Entropy Concept and Its Application in Engineering Test," *Machine Tool & Hydraulics*, vol. 3, pp. 259–261, 2003.

[30] D. Datta and N. N. Kishore, "Features of ultrasonic wave propagation to identify defects in composite materials modelled by finite element method," *NDT & E International*, vol. 29, no. 4, pp. 213–223, 1996.